Applied Thermal Engineering 224 (2023) 120049

Contents lists available at ScienceDirect

Applied Thermal Engineering

journal homepage: www.elsevier.com/locate/apthermeng

Research Paper

Mixing performance of preheated flue gas entering selective catalytic reactor under low loads

Yize Zhang, Mingrui Zhang, Hao Zhou *

State Key Laboratory of Clean Energy Utilization, Institute for Thermal Power Engineering, Zhejiang University, Hangzhou 310027, China

A R T I C L E I N F O

Keywords:
Low load
Multiple jets
Mixing performance
Velocity ratio
Flow charge distribution characteristic

A B S T R A C T

The reduced inlet flue gas temperature of the selective catalytic reduction (SCR) denitrification device is a significant problem during the low-load operation of boilers. In this study, an experimental system for turbulent thermal mixing of high and low-temperature flue gases was built to study the thermal mixing method in bypass flue gas technology and the effect of the temperature difference and flow rate variation of high and low-temperature flue gases at low load on the thermal mixing characteristics. The experiments evaluated the thermal mixing characteristics by measuring the temperature field distribution, calculating the inhomogeneity parameters ζ_T, and investigate the multi-jet distribution characteristics. The investigation was carried out more accurately by combining the simulation results. The results show that the tube wall jet combined with the bottom jet method provides the highest warming effect and possesses the lowest mixing non-uniformity parameter. At the location which is 1.25 times the hydraulic diameter of the duct away from the jet pipe, the temperature difference between the mainstream and the jet drops from 270 °C to 180 °C, causing ζ_T to drop from 0.46 to 0.37. Decreasing the jet velocity and increasing the main flow velocity promote a decrease in ζ_T, indicating that the ratio of jet velocity to main flow velocity and the velocity ratio $\frac{U_J}{U_m}$ are crucial factors affecting the thermal mixing characteristics, which directly affects the heat transfer between hot and cold fluids. The ζ_T decreases from 0.52 to 0.42 as $\frac{U_J}{U_m}$ changes from 3.58 to 2.15. This study provides a reference for ensuring the safe and stable operation of SCR denitrification system during the low-load operation of coal-fired boilers.

1. Introduction

Recently, carbon emission reduction has become a new requirement for industrial development. New clean energy sources are rapidly developing, with the percentage of installation and power output increasing annually [1–3]. However, new energy sources, such as solar power, wind power, and hydroelectric power generation, are characterised by unstable power generation. This is because they are subject to natural conditions, resulting in fluctuations in the of power generation capacity [4,5]. To meet electricity demand, the electricity grid must regulate the electricity production. Thermal power is the backbone of the power industry in China. As China remains the primary global coal producer and user, coal will continue to play an irreplaceable role in China's energy consumption for some time in the future [6,7]. Following China's energy development policy, coal-fired generating units must provide flexible peaking capabilities to guarantee the long-term stable and safe operation of coal-fired power plant systems under low loads[8]. However, during the operation of thermal power units under low-load conditions (generally below 50 % of the rated load), the flue gas temperature from combustion decreases. Selective catalytic reduction (SCR) denitrification technology is now widely used in power plants to remove pollutants from flue gases. The catalysts used in this technology operate in the temperature range of approximately 280 to 420 °C [9]. NH3 produced by the reducing agent reacts with SO3 in the flue gas to form ammonia sulfate or ammonia bisulfate when the SCR inlet flue gas temperature is below the catalyst operating temperature. The ammonium salts generated block the catalyst's active micro-pores, which causes abrasion and reduces catalyst activity, resulting in reduced catalytic efficiency, higher NOx emissions, and increased ammonia escape [10–13]. These problems can be solved by improving the inlet flue-gas temperature of the SCR device through a flue gas bypass or by developing catalysts for the low-temperature range[14,15]. The conventional flue gas bypass method injects high-temperature flue gases directly into the low-temperature flue gases of the main tail flue, as illustrated in Fig. 1, but the high- and low-temperature flue gases fail to mix uniformly

---

* Corresponding author at: State Key Laboratory of Clean Energy Utilization, Zhejiang University, Zheda Road 38, Hangzhou 310027, China.
E-mail address: zhouhao@zju.edu.cn (H. Zhou).

https://doi.org/10.1016/j.applthermaleng.2023.120049
Received 6 October 2022; Received in revised form 5 January 2023; Accepted 10 January 2023

Nomenclature

D_h	hydraulic diameter, mm
W	wetted perimeter, mm
U_J	jet velocity, m/s
Um	mainstream velocity, m/s
ρ_J	jet gas density, kg/m^3
ρ_m	mainstream gas density, kg/m^3
A_J	cross-sectional area of jet inlet, m^2
A_m	cross-sectional area of the main flue, m^2
R	velocity ratio, $R = Um / U_J$, dimensionless
R_m	flow ratio, $R_m = \rho_J A_J U_J / \rho_m A_m U_m$, dimensionless
Φ	jet hole diameter, mm
N	number of the jet holes
x_n	calculation results
L	length of jet pipe in the flue, mm
P_r	pressure to the right of the jet hole, Pa
P_l	pressure to the left of the jet hole, Pa
K	static pressure change factor
λ_l	friction coefficient inside jet tube
V_l	velocity to the left of the jet hole, m/s
V_r	velocity to the right of the jet hole, m/s
D	distance between adjacent holes, m
D_H	jet hole diameter, m
D_P	inner diameter of the jet pipe, m
P_{out}	external environmental pressure, Pa
β	local resistance coefficient
V_J	jet hole flow velocity, m/s
ζ_T	inhomogeneity parameter of temperature distribution
T	time-averaged temperature of each measurement point, ℃
T_0	mainstream temperature, ℃
T_{max}	maximum temperature within the y/Dh = 1.25 cross-section, ℃
σ_T	standard deviation of the measured temperatures on the surface
θ	dimensionless temperature in the measurement plane
ΔT	temperature difference, ℃
R_{eff}	effective velocity ratio

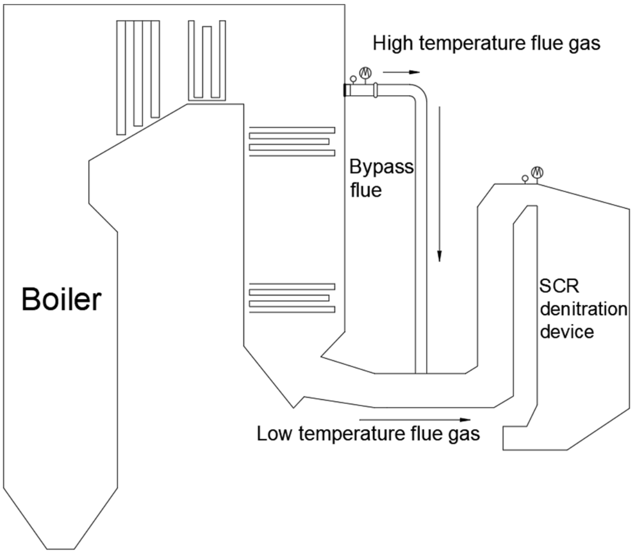

Fig. 1. Schematic diagram of flue gas bypass heating technology.

over short distances. Because the reactivity of the catalyst is very temperature-sensitive, temperature deviations at the SCR inlet flue can still lead to higher NOx emissions [16]. Therefore, the flue gas injected into the SCR denitrification system must not only meet the specific temperature of the operating range but also ensure the uniformity of heat distribution to achieve safe and reliable functioning of coal-fired station systems under low loads [17].

The traditional bypass flue gases thermal mixing of hot and cold flue gas mentioned above is the essence of the physical phenomenon of jet into crossflow (JICF). This classical fluid motion is characterised by complex flow and mixing characteristics [18]. Researchers have conducted studies in related areas. Su et al. [19] measured the time-averaged turbulence values and velocity fields of round-hole jets in the developing region of the flow using planar laser-induced fluorescence (PLIF) and particle image velocimetry (PIV) techniques and analysed the scaling properties of the JICF. Naik-Nimbalkar et al. [20] studied the thermal mixing of the crossflow of double jets in the same row by experimental and numerical simulations, measured time-averaged speeds and temperature fields, and predicted the temperature undulations using temperature variance models. Ghahremanian et al. [21] used PIV and laser doppler anemometry (LDA) to study the near-field confluence characteristics of a 6 × 6 inline circular nozzle arrangement at low Reynolds number. The flow field of the converging jets exhibited an asymmetrical distribution of Reynolds stress around the jet axis and highly anisotropic turbulent flow. Choi et al. [22] analysed the variation law of the intrusion performance of a secondary air injection system with the jet intrusion factor and momenta flux ratio through visualisation experiments. Zhou et al.[23] investigated the mixing process and distribution characteristics of a supercritical endothermic hydrocarbon fuel jet in a supersonic crossflow, using both experimental and numerical methods. The study reveals the effects of conditions such as the inflow Mach number, injection pressure, and injection temperature on the mixing efficiency. Wang et al. [24] conducted an experimental study of a water jet injected laterally into a subsonic crossflow using digital holographic imaging and explored the relationship between the jet column trajectory and downstream droplet distribution. Lv et al. [25] investigated the evolution of different vortex structures in cross-flow jets and their interaction mechanisms using high-precision numerical methods, and further investigated the effect of the velocity ratio on the vortex structure.

JICF is widely used in engineering practices such as combustion instability control [26,27], pollutant generation regulation [28–31], and cooling of gas turbine gas films [32]. Zhou et al. [28] investigated the impact of N_2/O_2 and CO_2/O_2 jets on the combustion instability, diluted premixed methane flame structures, and NO_X emissions. The results showed that the CO_2/O_2 jet produced a more homogeneous temperature field than the N_2/O_2 jet, resulting in reduced NO_X emissions. Stiehl et al. [29] investigated the effect of N_2 and CO_2 diluents contents on NO and CO emissions in crossflow premixed reaction jets, revealing a relationship between diluents addition, axial exotherms, and nitric oxide contamination generation. Zhu et al.[33] simulated and compared the influence of internal coolant crossflow in a novel film cooling hole design, called “sister holes”, and a baseline cylindrical hole, which found the air film cooling performance of the sister hole was better than that of the reference cylindrical hole under different blowing ratios, and the advantage of the sister hole was obvious with the increase of the blowing ratio. Ding et al.[34] introduced porosity into the Navier-Stokes equation and developed a procedure to solve gas-particle two-phase flow in a supersonic flow field. The evolution of the vortex structure, hydrogen/metal powder fuel distribution, jet penetration depth and mixing efficiency in single- and two-hole jet flow fields in a supersonic crossflow were analysed. Little research has been conducted on increasing the SCR

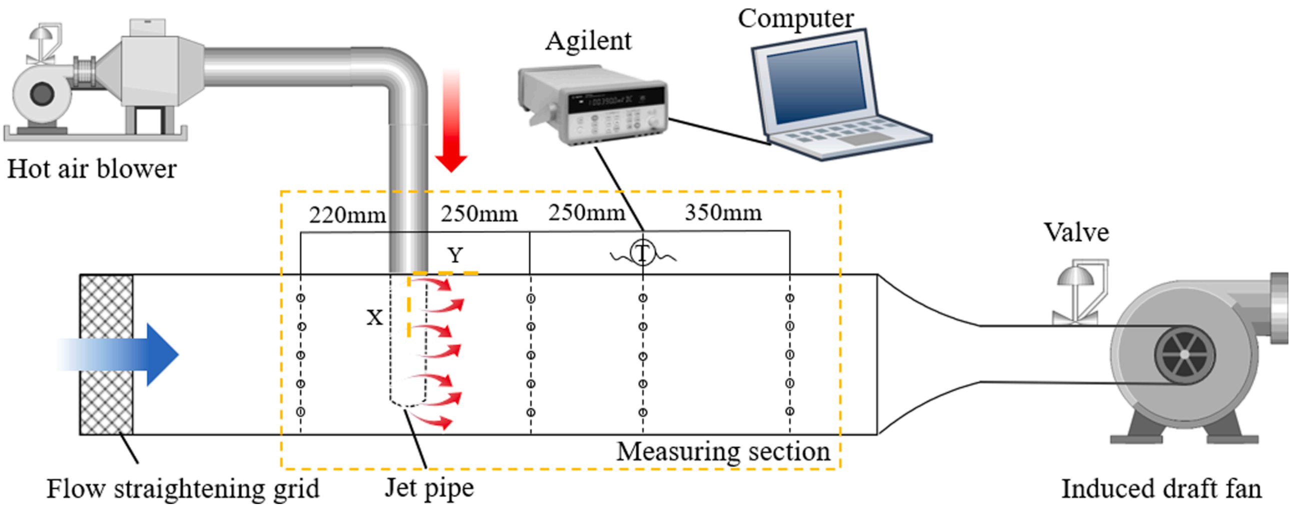

Fig. 2. Schematic diagram of experimental setup.

Table 1
Experimental cases.

Case	Main flow temperature (℃)	Jet flow temperature (℃)	Temperature difference (℃)	Main flow velocity (m/s)	Jet flow velocity (m/s)	$R=\frac{U_J}{U_m}$	$R_m=\frac{\rho_J A_J U_J}{\rho_m A_m U_m}$ (%)	Type
1	35	305	270	8	25	3.13	19.63 %	a
2	35	305	270	8	25	3.13	19.63 %	b
3	35	305	270	8	25	3.13	19.63 %	c
4	35	260	225	8	25	3.13	19.63 %	a
5	35	215	180	8	25	3.13	19.63 %	a
6	35	305	270	8	18	2.25	14.14 %	a
7	35	305	270	8	21.5	2.69	16.89 %	a
8	35	305	270	6	21.5	3.58	22.51 %	a
9	35	305	270	10	21.5	2.15	13.51 %	a

Fig. 3. Different types of jet mixing.

inlet temperature by thermally mixing high- and low-temperature flue gases with multiple jet pipes in coal-fired power plants under low-load operation. Zhou et al. [35] proposed a multi-jet flue gas mixing method to preheat sintered flue gas and investigated its thermal mixing behaviour. Guo et al. [36]investigated the thermal mixing effect of a preheated sintering gas in perforated tubes with several inclined jet angles. The results showed that the best mixing performance was achieved with an angular configuration of 120° between the jet holes. However, current studies do not apply to coal-fired boilers operating at low loads. The flue gas of pulverised coal furnaces at low loads contains a large amount of fly ash. The ash particles of the high-temperature flue gas that hit the low-temperature wall can be deposited and attached to the surface [37], continuously growing and eventually forming slag to block the openings of the jet pipe wall.

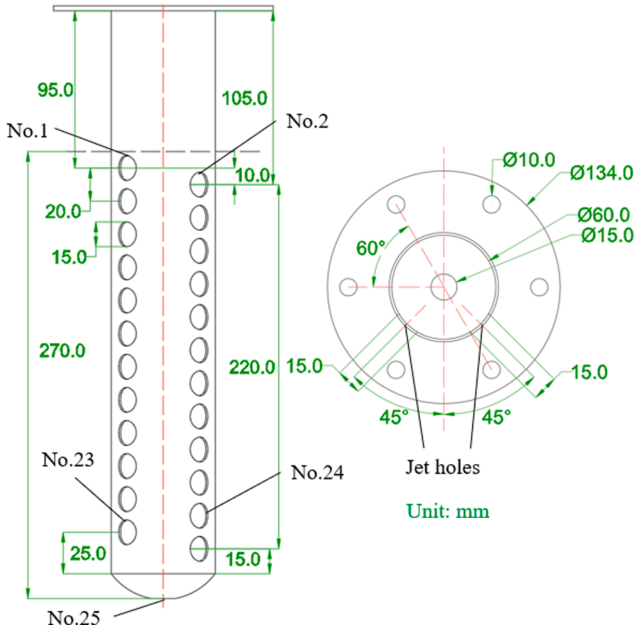

Fig. 4. Schematic diagram of the multihole jet pipe (a).

In this study, two novel multi-jet structures were proposed for the

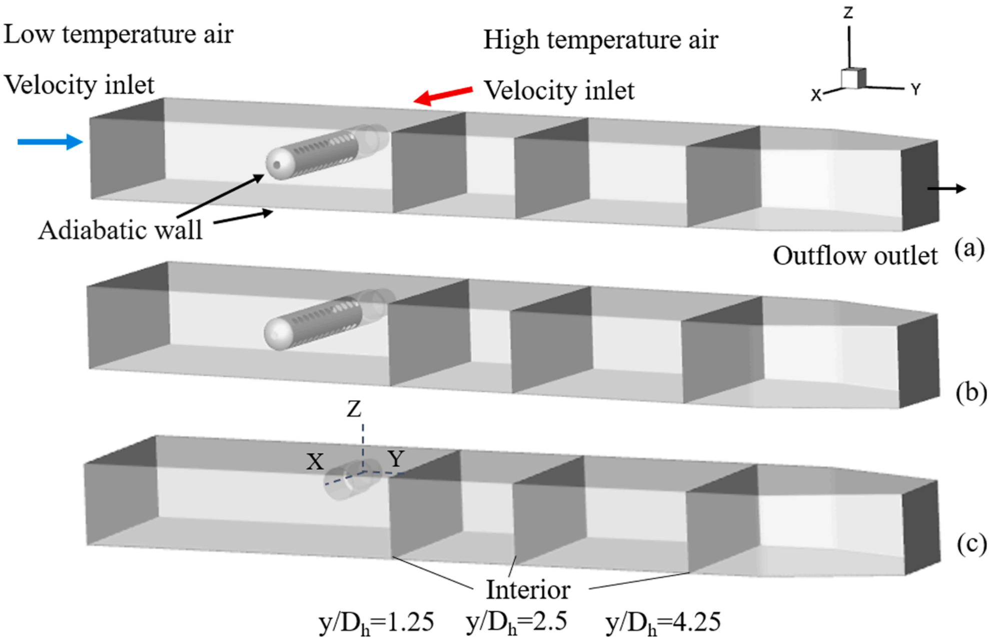

Fig. 5. Simulated geometry and boundary conditions of the experimental subject.

Table 2
Grid independence test and verification results (Case 1).

Grid	y/D_h = 1.25 surface average temperature(K)	Error (%)	y/D_h = 2.5 surface average temperature(K)	Error (%)	y/D_h = 4.25 surface average temperature(K)	Error (%)	y + Max.
129,106	332.3656	–	328.6326	–	327.4716	–	236.51
320,986	331.0990	0.38 %	328.0623	0.17 %	327.0295	0.13 %	191.43
861,476	331.6189	0.16 %	328.8845	0.25 %	327.3786	0.11 %	120.28
1,271,069	331.9955	0.11 %	329.0661	0.06 %	327.5379	0.05 %	104.01
2,154,111	331.9452	0.09 %	328.9762	0.03 %	327.4409	0.04 %	91.08
4,921,617	333.6555	0.52 %	329.5200	0.17 %	327.7025	0.08 %	74.34

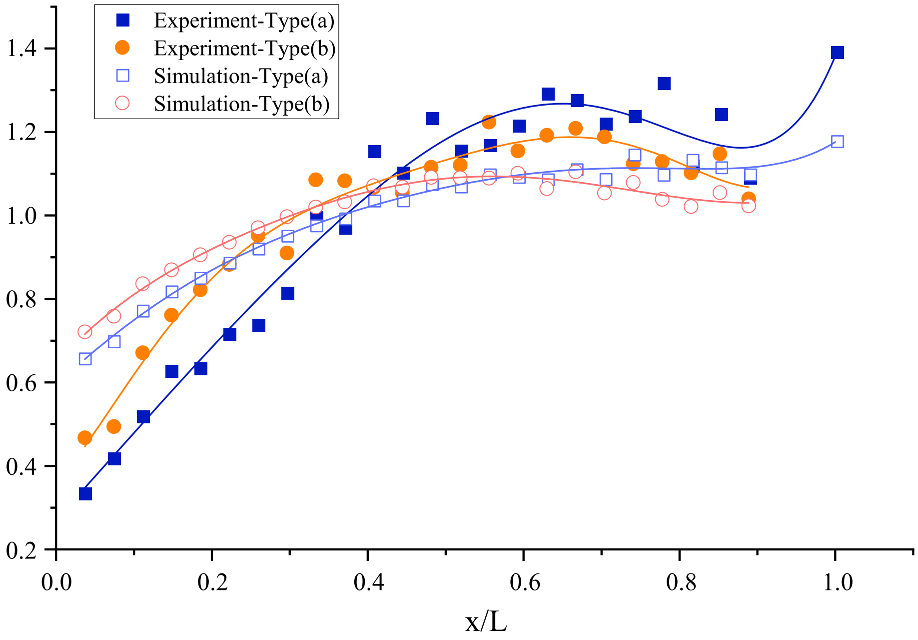

Fig. 6. The dimensionless jet velocity distribution characteristics along the jet pipe.

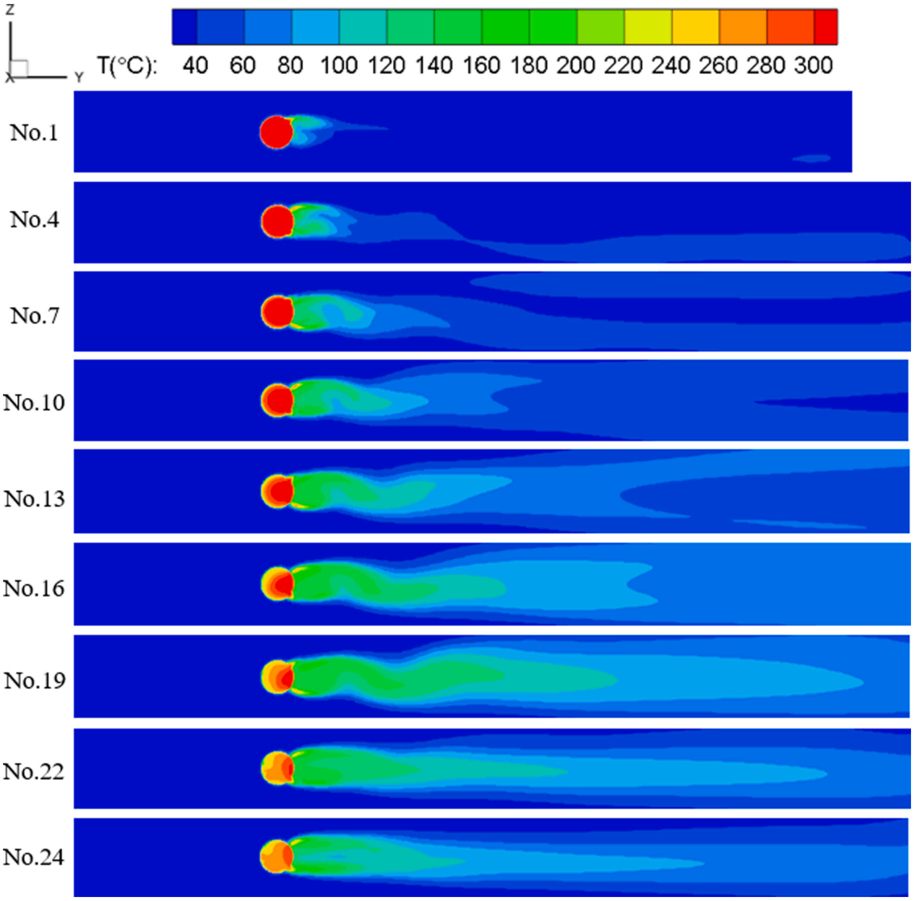

Fig. 7. Temperature contours of the transverse section in the centre of partial jet holes.

thermal mixing of high-and low-temperature flue gases, and the jet distribution characteristics were investigated. An experimental system was built to simulate preheating of the inlet flue gas of an SCR denitrification unit in a coal-fired power plant by extracting high-temperature flue gas through a bypass flue. This study compares the mixing performance of different hot flue jets with that of the mainstream. The influence of the temperature difference and flow velocity variation of the flue gas in the main flue and bypass flue on the flue gas thermal mixing characteristics under low load conditions was investigated. In practical engineering applications, many injection stubs are installed at the lower end of the bypass flue and are inserted into the main flue. Due to the symmetrical nature of pipe placement, the present experimental and simulation studies focused on a single-branched pipe. This study provides a reference for ensuring the safe and reliable operation of SCR denitrification systems for coal-fired boilers under low loads.

2. Experimental setup

2.1. Experimental device

The experimental setup is illustrated in Fig. 2. The subject of the experimental model was a main flow duct with a rectangular cross-section, and the horizontal side position was installed with a multi-hole jet pipe. To simulate engineering reality, the experimental model size was scaled down to 1:10. The jet pipe was installed horizontally in a rectangular main duct attached to a hot-air blower at the rear end. The main flow duct has a cross-sectional area of 300 mm × 150 mm, with hydraulic diameter equal to $D_h = 200$ mm. The formula for calculating D_h is shown in Eq. (1).

$$D_h = 4\frac{A_m}{W} = 4 \times \frac{150 \times 300}{2(150 + 300)} = 200mm\# \tag{1}$$

where A_m represents the transverse area of the main flue and W represents the wetted perimeter.

In a hot-gas production system, high-temperature air is provided by a hot-air blower. The inlet air temperature was controlled by adjusting the heating power of the hot air blower, and the air valve regulated the airspeed (air volume). Upstream from the main pipe, a flow straightening grille was used to rectify and homogenise the main flow. The induced draft fan controls the airflow rate in the main duct.

The measurement section contained four measurement planes along the main wind tunnel, with five sampled holes at the upper part of each plane and three sampled holes on the right side. The origin of the coordinate system of the device (0, 0) is located at the junction of the axis of the jet pipe and the left interface of the main windpipe. The X-axis is paralleled to the jet pipe, and the Z-axis is parallel to the altitude direction. The four measurement planes were positioned at Y = -220 mm, 250 mm, 500 mm, and 850 mm. The first measurement plane is used to verify the uniformity of the gas-stream distribution before it passed over the jet pipes.

2.2. Experiment case

According to the available data for a coal-fired boiler, the flue gas temperature difference between the exit of the final superheater and the outlet of the economiser during low load operation is the lowest at 180 °C and can increase to 270 °C. The locations are used for extracting high-temperature flue gas and low-temperature mainstream flue gas sources. Therefore, the following study cases were set up as detailed in

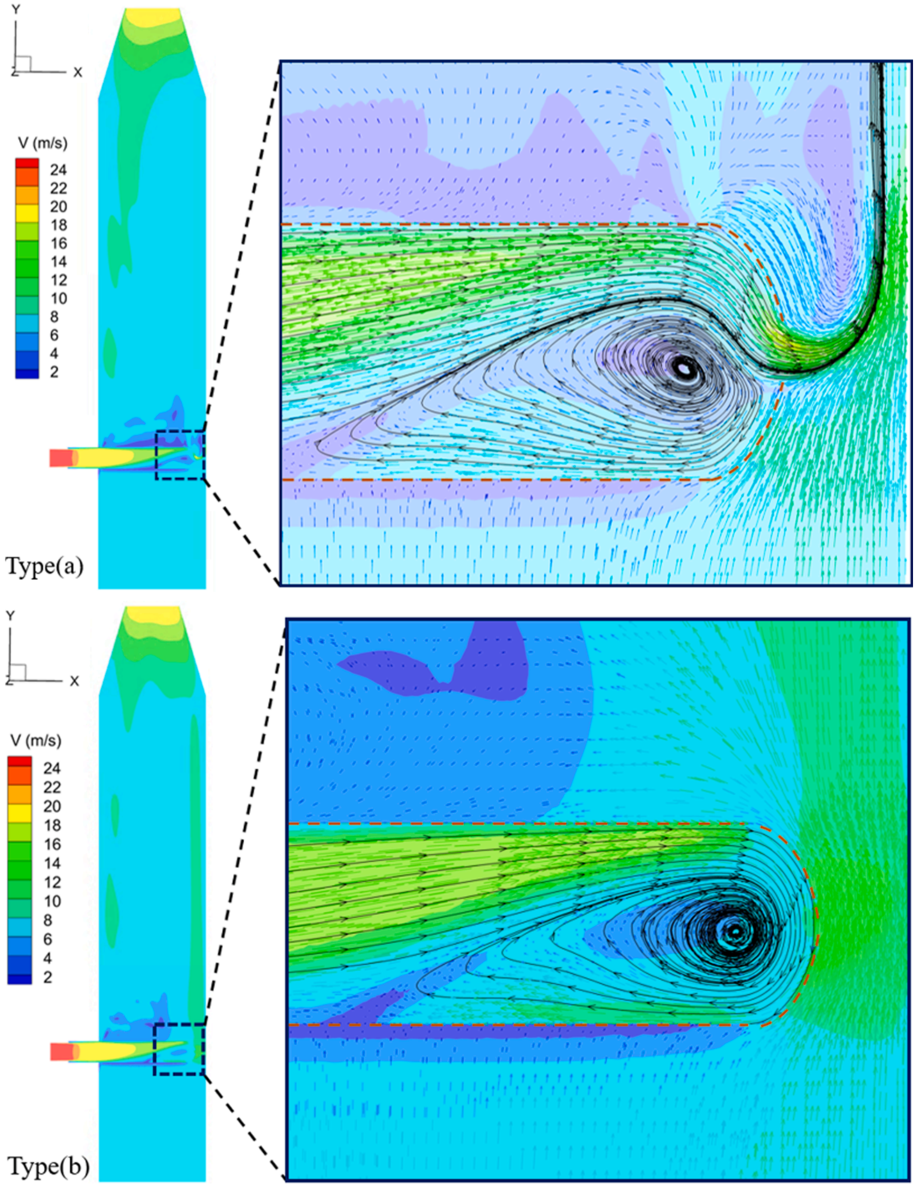

Fig. 8. Velocity contours and streamlines inside the jet pipe.

Table 1.

Cases 1–3 compared three different types of high-temperature flue gas injection methods, including two types of multi-jet and a single jet injected as a jet in crossflow. The actual structure is shown in Fig. 3. The diameter of the jet pipe was 60 mm, and 24 jet holes were opened on the wall of the pipe. The inner diameter of the jet holes was $\Phi = 15$ mm, and the jet holes on the wall of the pipe were staggered in two rows at equal distances. The angle between each row and the centre axis of the pipe was $\alpha = 45^\circ$, and the adjacent jet holes were separated by 20 mm. When installing the jet pipe, keep the central surfaces of the two rows of jet holes horizontal. The dimensions are shown in Fig. 4. A flange was welded to the base of the jet pipe as a connection to an inlet pipe mounted on the side of the pipe. Jet pipe (a) contains a bottom centre jet hole with an inner diameter of 15 mm in addition to the jet holes in the wall, which is a total of 25 holes. These bottom centre jet holes are employed in engineering practice to blast the ash particles in the flue gas from the jet pipe, preventing the jet holes in the pipe wall from becoming clogged by ash accumulation. Jet pipe (b) has only jet holes in the pipe wall. Type (c) is a single jet. The main flow duct was 300 mm wide, and the length of the jet pipes (a) and (b) deep into the main flow duct accounted for 90 % of the duct width, which was 270 mm, to reduce the production cost and ensure adequate outflow of the bottom jet. A jet pipe was installed in the main flow duct, with jet holes on the backwind side. The centres of the two lines of the jet holes were maintained in the same vertical section.

2.3. Scalar field measurement

The flow distribution through the jet holes of the multihole pipes was measured using a hot-wire anemometer (KAMOMAX), which provided a measurement accuracy of ± 3.0 % and a measurement precision of 0.01 m/s. The time-averaged temperature was measured using K-type thermocouples attached to Agilent with an accuracy of ± 1.5 °C. Fifteen thermocouples were used to obtain the vertical temperature distribution within the mainstream pipe. Similarly, 18 thermocouples were arranged horizontally to measure the average temperature over two minutes. The Agilent data-acquisition frequency was 2 Hz. Up to 129 measurement points in each measurement plane were available for the data processing.

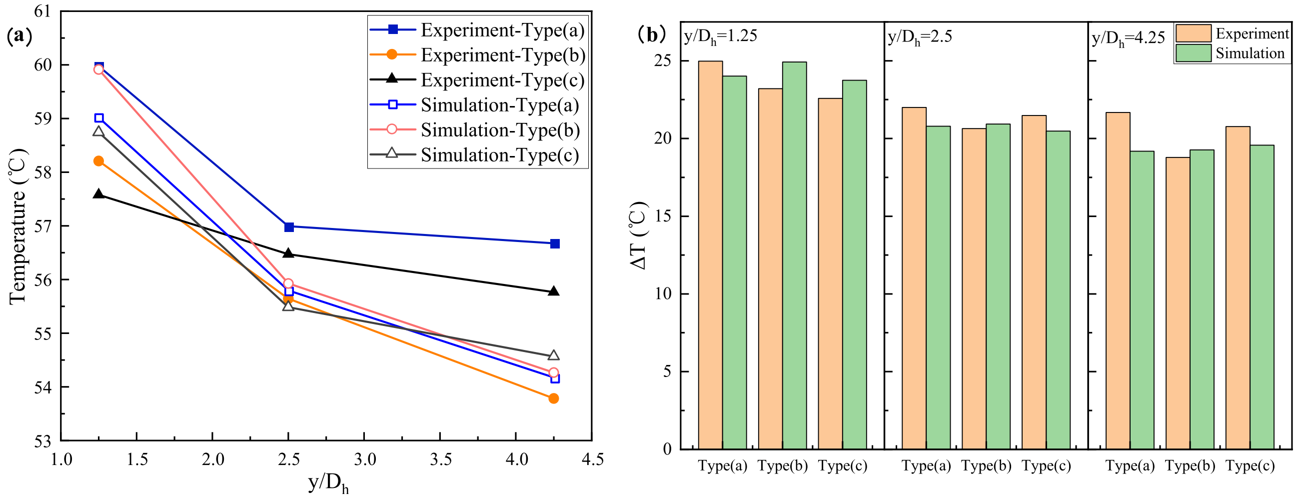

Fig. 9. Effect of thermal mixing of different jet types on the axial temperature. (a) The average temperature of each section after thermal mixing; (b) the average warming effect of each section after thermal mixing.

3. Simulation

To ensure the accuracy of the experimental results, further investigations employing computational fluid dynamics (CFD) numerical simulations were performed. The steady-state flow of an incompressible fluid was considered, and the effect of radiative heat transfer was neglected. Therefore, the governing equations are expressed as follows.

The continuity equation:

$$\frac{\partial(\rho u_i)}{\partial x_i} = 0\# \tag{2}$$

The momentum equation:

$$\frac{\partial(\rho u_i u_j)}{\partial x_i} = -\frac{\partial P}{\partial x_i} + \frac{\partial}{\partial x_i}\left[(\mu+\mu_t)\left(\frac{\partial u_j}{\partial x_i}+\frac{\partial u_i}{\partial x_j}\right)\right]\# \tag{3}$$

The energy equation:

$$\frac{\partial(\rho u_i T)}{\partial x_i} = \frac{\partial}{\partial x_i}\left[\left(\frac{\mu}{P_r}+\frac{\mu_t}{P_{r_t}}\right)\frac{\partial T}{\partial x_i}\right]\# \tag{4}$$

Numerical simulations were performed using the commercial software ANSYS-FLUENT 2020 R2, and the pressure-based solver was used to solve the nonlinear control equations. The computational model was based on the measurement part of the experimental system, and the inner diameter of the front tube of the jet port was 50 mm, which was the same as the inner diameter of the air supply end of the experimental system where the hot air fan and the porous jet tube were connected. The computational cases are consistent with the experimental conditions. The specific model structure and boundary conditions are shown in Fig. 5. In this simulation, the viscous model used the standard k–ε model with standard wall functions for the boundary layer problem, which provided reasonably accurate results for wall boundary flows with very high Reynolds numbers. The other wall surfaces were set as non-slip adiabatic walls. The SIMPLE algorithm solves the flow field. The second-order upwind scheme was used to discretise the convection term.

Three cross sections in the model with y/D$_h$ = 1.25, y/D$_h$ = 2.5 and y/D$_h$ = 4.25 were selected as check surfaces in the grid independence verification. The calculated values were compared and the errors were calculated. The total mesh size was increased by increasing the number of nodes. In the grid-independent validation, the jet pipe type of the model is as shown in (a). Table 2 lists the errors for the three cross-sections. The error was calculated using the following Eq. (5),

$$error = \frac{|x_n - x_{n+1}|}{x_n} \times 100\%\# \tag{5}$$

where x_n denotes the calculation result, and n indicates the *n*-th calculated case.

Table 2 shows that as the grid number increases from 129,106 to 2,154,111 the surface average temperature errors of the three cross sections become smaller and smaller. When the number of grids increases to 4921 1617, the error of the calculation results increases. When the number of grids increases from 861,476 to 2154111, the errors in the calculation results for all three inspection surfaces are within 0.2 %. Furthermore, the errors in the calculations are all within 0.1 % when the number of grids increases from 1,271,069 to 2154111, which is small enough to be negligible. Therefore, the grid number for all simulations was 1,271,069 to ensure accuracy while reducing computational time.

4. Results and discussion

4.1. Jets stream distribution features

The flow distribution of jet holes is influenced by factors such as the hole size, hole spacing, and location of the jet hole [35,36]. Differences in the flow distribution characteristics of different structural jet pipes can affect the penetration intensity of the jet in the mainstream [22], leading to changes in the thermal mixing performance of the high- and low-temperature flue gases. Therefore, an analysis of the jet stream distribution features of the different jet pipes is required. The results are shown in Fig. 6, where the dimensionless jet speed of the jet orifice tends to increase and then decays along the jet pipe. The extreme values appear between x/L = 0.6 and 0.8 in the middle and rear sections of the jet pipe.

Fig. 7 presents the temperature distribution in the centre transverse section of some jet holes during the thermal mixing of high and low-temperature gases in the (a)-type pipe. It can be visually observed that the high-temperature zone behind the jet pipe steadily expands from the 1st to the 19th jet hole, correlating with the gradually increasing jet flow from the jet hole at this point. From the 19th to the 24th jet hole, the high-temperature area behind the jet pipe gradually decreases, corresponding to a gradual decay of the jet flow from the jet hole at that location. The relative position of the 19th jet hole was x/L = 0.704, which was located between x/L = 0.6 and 0.8.

In comparison to pipe (b), pipe (a) had an additional bottom jet orifice. When the flow distributions of the (a) and (b) jet pipes are compared, the flow distribution of the (a) pipe deviates more meanwhile

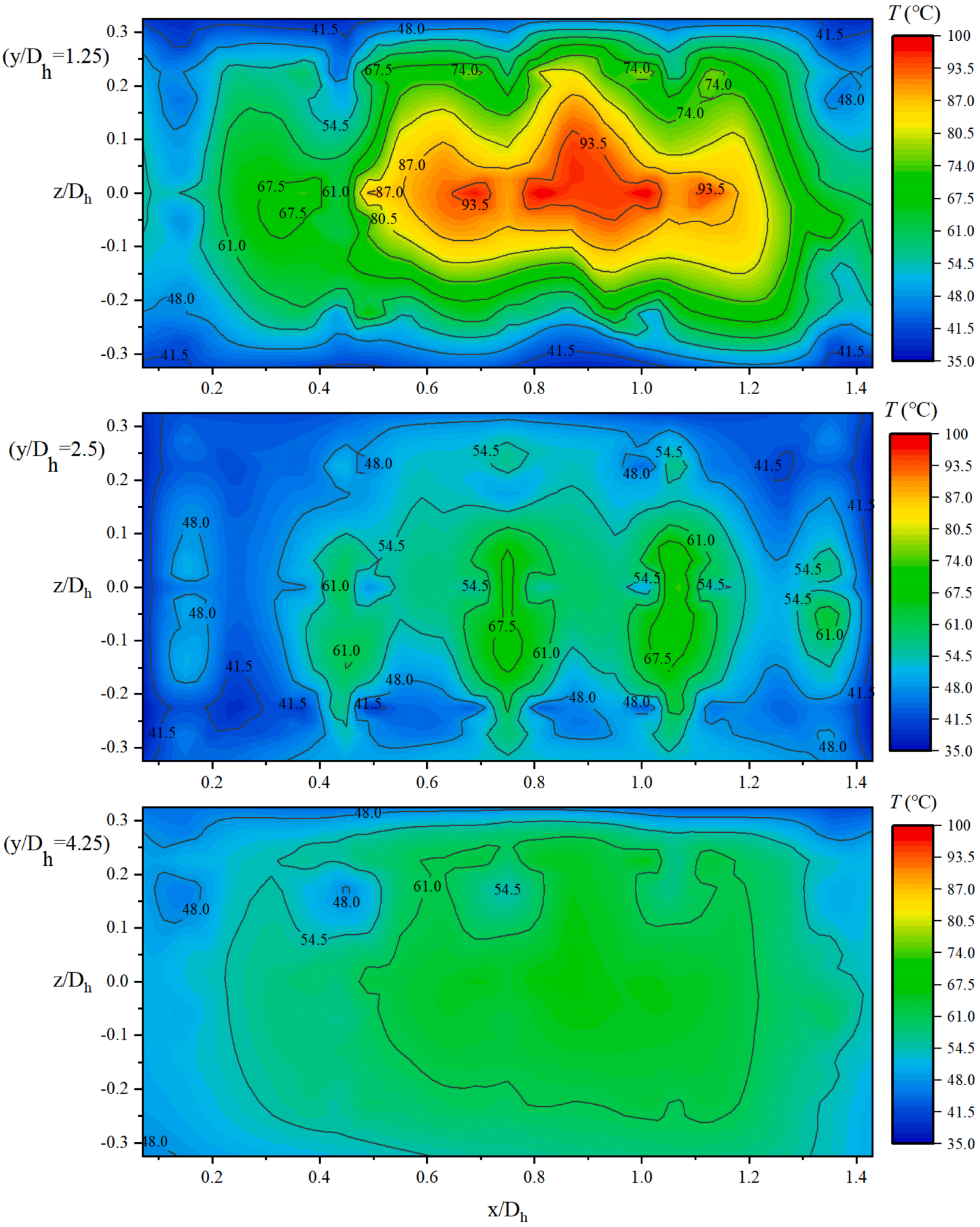

Fig. 10. Temperature distribution of case 1 (Type a) at y/D$_h$ = 1.25, y/D$_h$ = 2.5 and y/D$_h$ = 4.25.

the dimensionless jet velocity of the bottom jet orifice (No.25) of the (a) pipe is the greatest. The trend seen in the simulation calculation results is similar to that found in the experimental results. This feature is advantageous in engineering applications because the ash particles in high-temperature flue gas are blown out from the bottom jet orifice, preventing the ash particles from blocking the jet orifice on the tube wall.

The structure of the multihole jet pipe was similar to that of the manifold pipe. To infer the flow distribution in the manifold pipe, the flow distribution of the multi-hole jet pipe was analysed using the discrete model proposed by Lu et al. [38]. The discrete model is expressed by Eq. (6) below.

$$P_r(i) - P_r(i-1) = \rho K\left[V_l^2(i) - V_r^2(i)\right] - \Delta P_x - \lambda_l(i)\frac{L-D_H}{D_P}\frac{1}{2}\rho V_l^2(i)\# \tag{6}$$

$$\frac{1}{2}\left[P_{dl}(i) + P_{dr}(i)\right] = P_{out} + [1+\beta]\frac{1}{2}\rho V_J\# \tag{7}$$

where r and l represent the right and left sides of the *i* th jet hole, respectively, and K denotes the static pressure conversion factor, which is a correction coefficient for the pressure loss. λ_l indicates the friction coefficient inside the tube. L, D$_H$, and D$_P$ represent the spacing between adjacent holes, jet hole diameter, and inner diameter of the jet pipe,

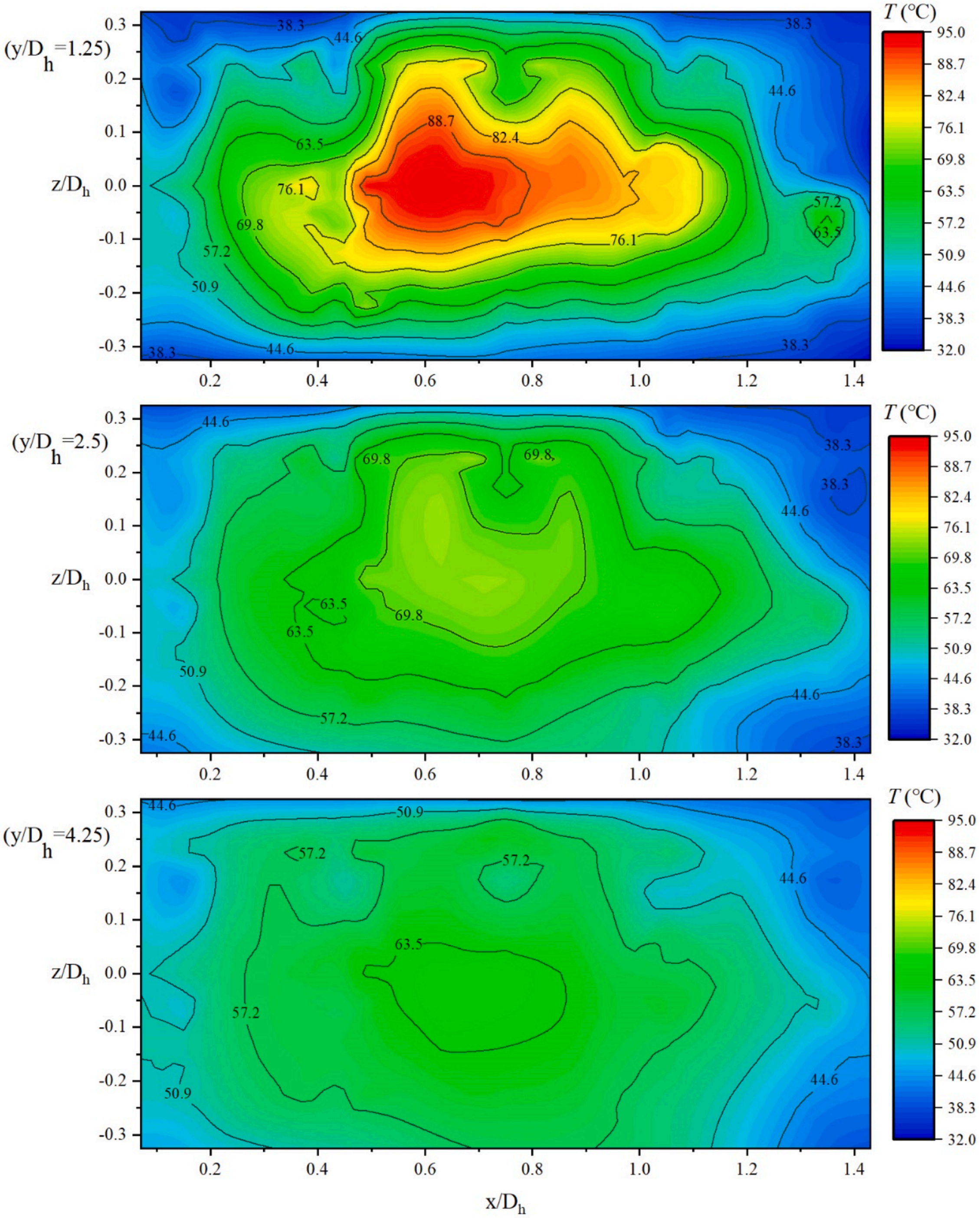

Fig. 11. Temperature distribution of case 2 (Type b) at y/Dh = 1.25, y/Dh = 2.5 and y/Dh = 4.25.

respectively.

In the above Eq. (6), the left side denotes the pressure drop between the adjacent jet holes, and the right side expresses the three factors that cause the pressure drop in this zone. The first term on the right is the pressure change induced by jet splitting, and the second and third terms represent the pressure change due to frictional resistance at the jet hole and non-opening section, respectively. The static pressure in the tube decreased with the along-stream resistance but increased with the jet-splitting effect. The frictional resistance to gas flow due to the smooth pipe walls can be neglected. Therefore, the change in the static pressure in the tube was mainly due to the splitting effect of the jet. The internal flow velocity of the pipe decreased along the jet direction, and the static pressure increased. By applying Bernoulli's equation to the jet hole, β in Eq. (7) represents the local resistance coefficient of the jet hole and P_{out} is the external pressure. The jet hole flow velocity increased with the static pressure inside the pipe, which means that the flow velocity of the jet hole increased along the direction of the jet in the pipe. Zhou et al. [35] studied the flow distribution characteristics of a multi-hole jet pipe with a flat bottom, and the experimental results were consistent with theoretical analysis.

The bottom of the jet pipe used in the experiment had a circular bore structure. According to the simulation results for analysing the path lines of a fluid particle in the tube, the front section between x/L = 0–0.6 had a path line distribution similar to that of the multi-hole jet tube with a

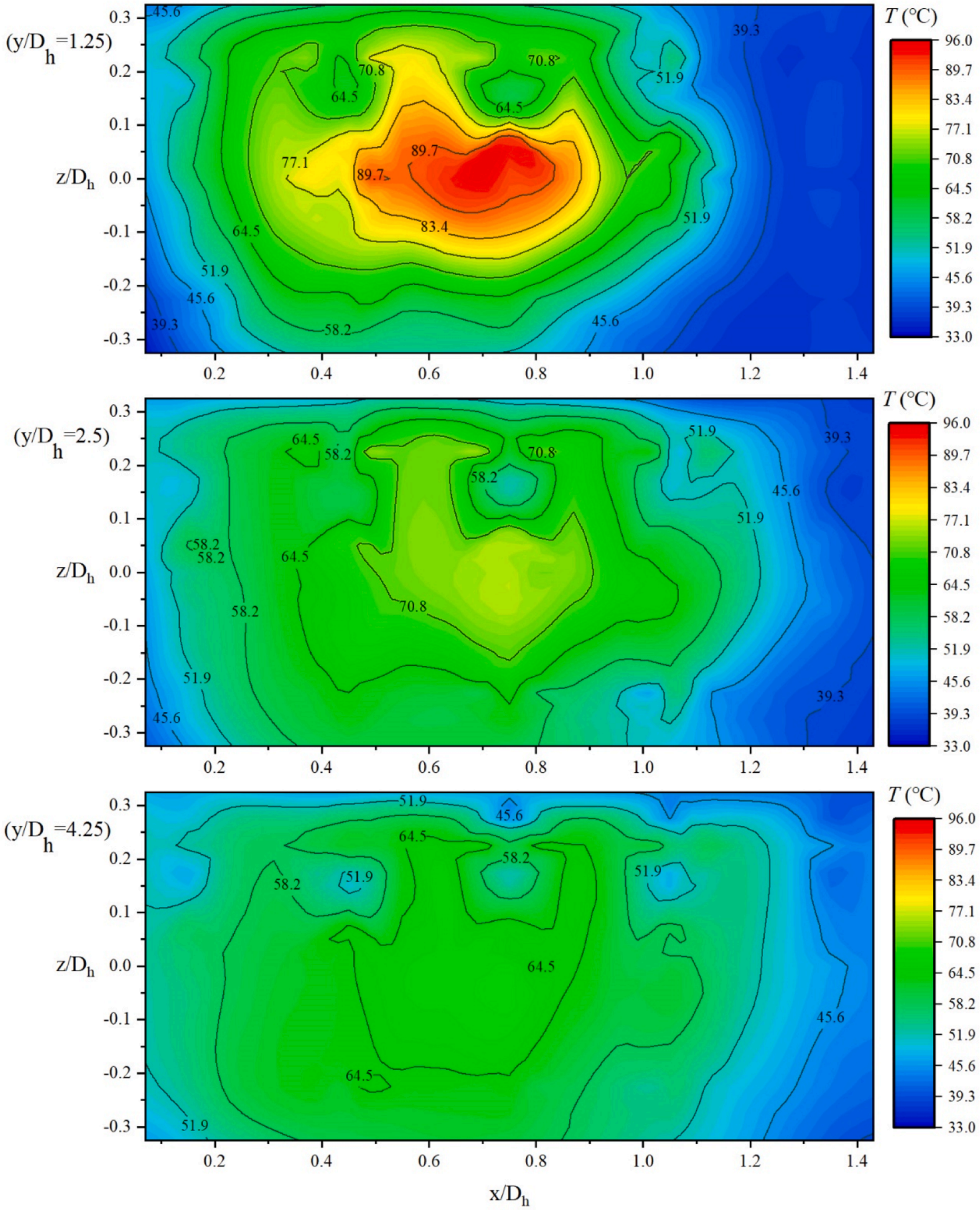

Fig. 12. Temperature distribution of case 3 (Type c) at y/D$_h$ = 1.25, y/D$_h$ = 2.5 and y/D$_h$ = 4.25.

flat bottom; therefore, the dimensionless jet velocity distribution of the jet hole in this region shows an increasing trend along the jet direction. Fig. 8 shows that in the latter section, between x/L = 0.6 and 1.0, an apparent recirculation zone appears, which affects the splitting effect of the jet hole and causes the jet hole flow velocity to decrease. This is an important reason why the dimensionless jet velocity distribution of the jet orifice tends to first increase and then decay.

4.2. *Jets stream temperature field distribution features*

Fig. 9 shows the effect of the three different jet types on the average axial surface temperature after mixing. At y/D$_h$ = 1.25 cross-section, the surface average temperature of types (a) and (b) after mixing is higher than that of type (c). However, the temperature after the thermal mixing decreased as the distance increased. At y/D$_h$ = 4.25 cross-section, the temperature after thermal mixing of type (b) was lower than that of type (c), while the warming effect of type (a) remained the highest.

Figs. 10-12 represent the time-averaged temperature distribution after the thermal mixing of the three different jet types within the measuring surfaces of y/D$_h$ = 1.25, y/D$_h$ = 2.5 and y/D$_h$ = 4.25. Fig. 12 shows that thermal mixing with type (c) formed a distinct local high-temperature region near the jet injection position in the flue cross-section. In contrast, a distinct low-temperature region (x/D$_h$ > 1.1) is formed away from the jet inlet side, indicating that the jet is deflected prematurely by the action of the main flow, resulting in an uneven temperature distribution with high local temperatures and low average

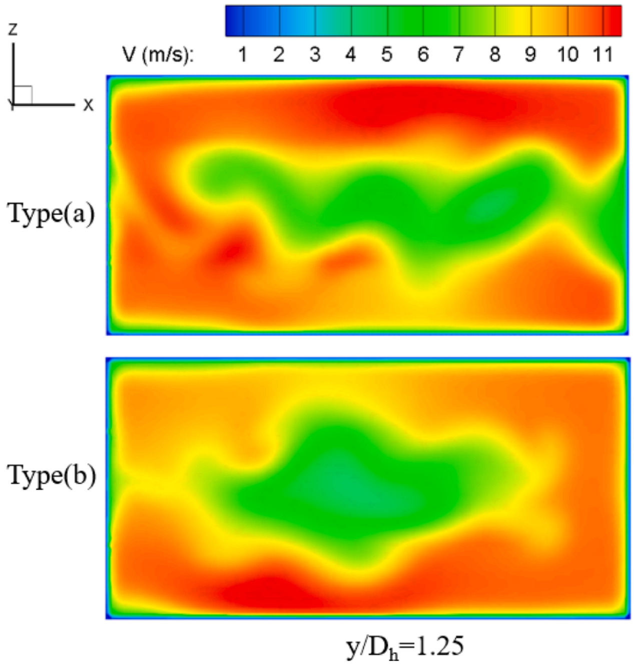

Fig. 13. Velocity distribution contours for case 1 (Type a) and case 2 (Type b) at y/D$_h$ = 1.25.

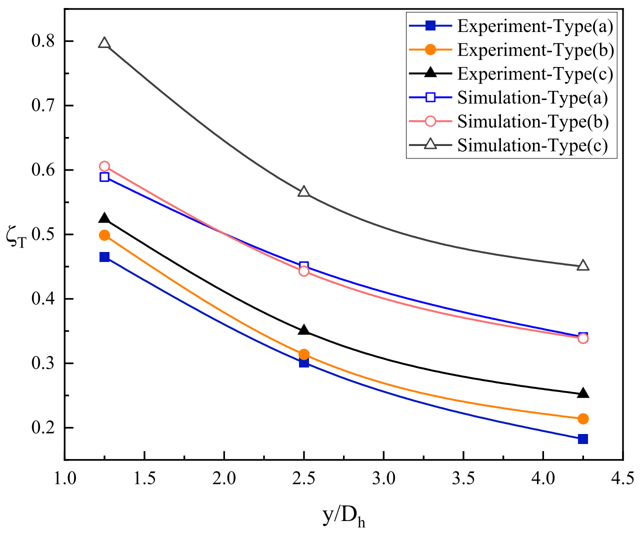

Fig. 14. Temperature mixing non-uniformity for different jet types.

surface temperatures.

As shown in Figs. 10 and 11, the high-temperature zones formed by the two methods of injecting high-temperature gases using multi-hole jet pipes are relatively distributed centrally in the middle of the cross-section, and the secondary high-temperature zones are uniformly distributed around, avoiding the existence of significant low-temperature zones. The multi-hole jet pipe prevents the hot gas stream from being prematurely wrapped by the main flow, as confirmed by Zhou et al.[35]. Fig. 10 shows that the high-temperature zone formed by thermal mixing of type (a) is mainly concentrated from x/D$_h$ = 0.8 to 1.0, corresponding to the position of x/L = 0.6 ~ 0.8 in the middle and rear sections of the jet pipe, which proves that the flow of high-temperature flue gas ejected from the jet hole at this location is high. The temperature gradient gradually increases between x/D$_h$ = 0 and 0.8, indicating that the flow rate of the jet hole increases with increasing x/D$_h$. This phenomenon is similar to that described above for the flow distribution characteristics of the jet pipe. A further comparison of Figs. 10 and 11 shows that in the range of x/D$_h$ > 1.1, a partial low-temperature region still exists, as shown in Fig. 11. This proves that the thermal mixing effect is better for the a-type pipe, and the opening of the jet holes at the bottom of the pipe plays a positive role in the thermal mixing process.

Fig. 13 shows the velocity distribution for types (a) and (b) at y/D$_h$ = 1.25, where it can be observed that the presence of the jet pipe leads to a low-pressure recirculation zone in the middle of the cross-section. Comparing (a) and (b), the low-velocity zone is more prominent in type (a) and reaches along the right edge of the main flue because the jet produced by the jet hole at the bottom of this position obstruct the main flow, causing a reduction in the axial flow velocity at this location. Therefore, the high-temperature zone in (a) can cover the right side of the pipe, and the temperature distribution effect is better than that in (b).

To investigate the inhomogeneity of the temperature distribution in the measurement planes after thermal mixing, the dimensionless parameter ζ_T was introduced to measure the inhomogeneity of the temperature distribution in the cross-sections within the flue.

This parameter is obtained by calculating all measurement points in the measurement plane. This enables an overall evaluation of the time-averaged temperature distribution, the validity of which has been verified in experiments by Lou et al. [39] and Guo et al. [36] The formulae are shown in Eqs. (8)–(10):

$$\zeta_T = \frac{\sigma_T}{\sqrt{\overline{\theta}(1-\overline{\theta})}}\# \tag{8}$$

$$\sigma_T = \sqrt{\frac{\left[\sum_{i=1}^{n}(\theta_i-\overline{\theta})^2\right]}{n}}\# \tag{9}$$

$$\theta = \frac{T-T_0}{T_{max}-T_0}\# \tag{10}$$

where T$_{\mathrm{max}}$ denotes the maximal temperature within all measured cross-sections., T$_0$ refers to the mainstream temperature, and T is the time-averaged measured temperature of each measuring point. θ represents the non-dimensional temperature in the measurement planes, and $\overline{\theta}$ is the average value of the non-dimensional temperature θ. θ takes values in the range 0–1. σ_T represents the overall standard deviation of the measured temperatures on the surface. When the hot and cold gases are entirely unmixed, σ_T is at its maximum value, $\sigma_T = \overline{\theta}(1-\overline{\theta})$, and when they are completely mixed, σ_T is at its minimum value, $\sigma_T = 0$. Therefore, the value of ζ_T is considered to range from 0 to 1. $\zeta_T = 0$ indicates that the temperature values are the same at all locations within the cross-section, achieving perfect mixing. $\zeta_T = 1$ indicates that the hot and cold gases are entirely unmixed and exhibit the most inhomogeneous temperature distribution.

According to Fig. 14, the experimental results indicate that type (a) has the lowest temperature non-uniformity coefficient among the three injection methods after mixing, with $\zeta_T = 0.18$ for type (a) and the highest temperature non-uniformity coefficient for type (c) within the y/D$_h$ = 4.25 cross-section, which is consistent with the simulation results. The ζ_T decreases as the mixing distance increased. Further comparing the experimental mixing results of type (a) and type (b), type (a) shows lower inhomogeneity coefficients than type (b) in all three measurement planes, and the results of the simulations indicate that the ζ_T of both are very close to each other, and the ζ_T of type (a) is below type (b) in the y/D$_h$ = 1.25 and 4.25 measurement planes. Therefore, it is reasonable to believe that thermal mixing in type (a) is the most effective and that the opening of the jet hole at the bottom contributes to the thermal mixing of high- and low-temperature flue gases. In addition, the temperature non-uniformity coefficients values calculated from the simulation

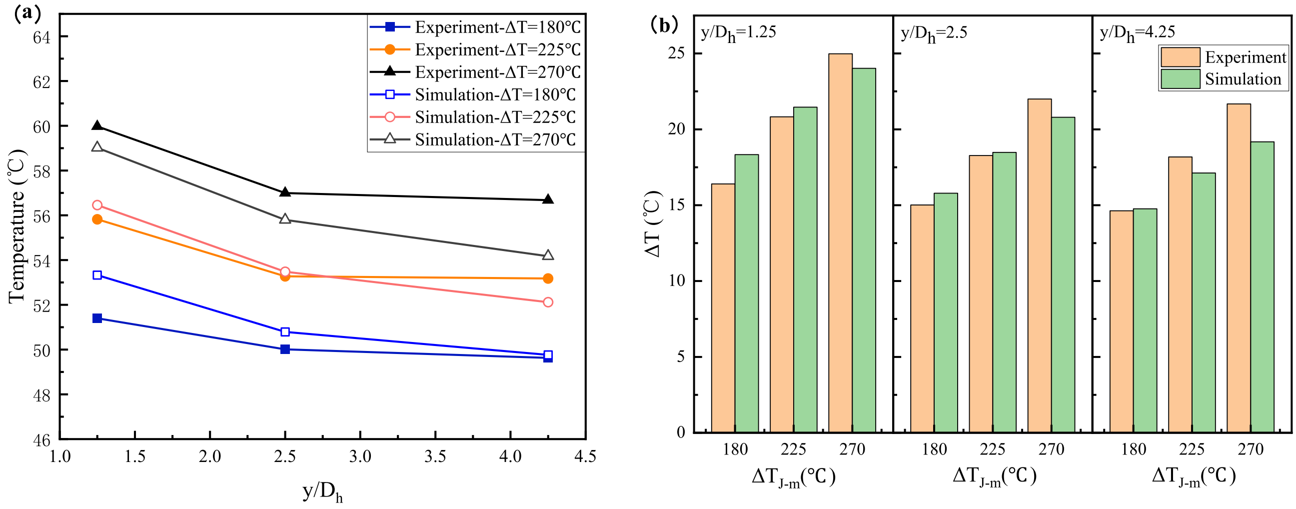

Fig. 15. Effect of the temperature difference between the main flow and the jet on the axial temperature after mixing. (a) The average temperature of each section after thermal mixing; (b) the average warming effect of each section after thermal mixing.

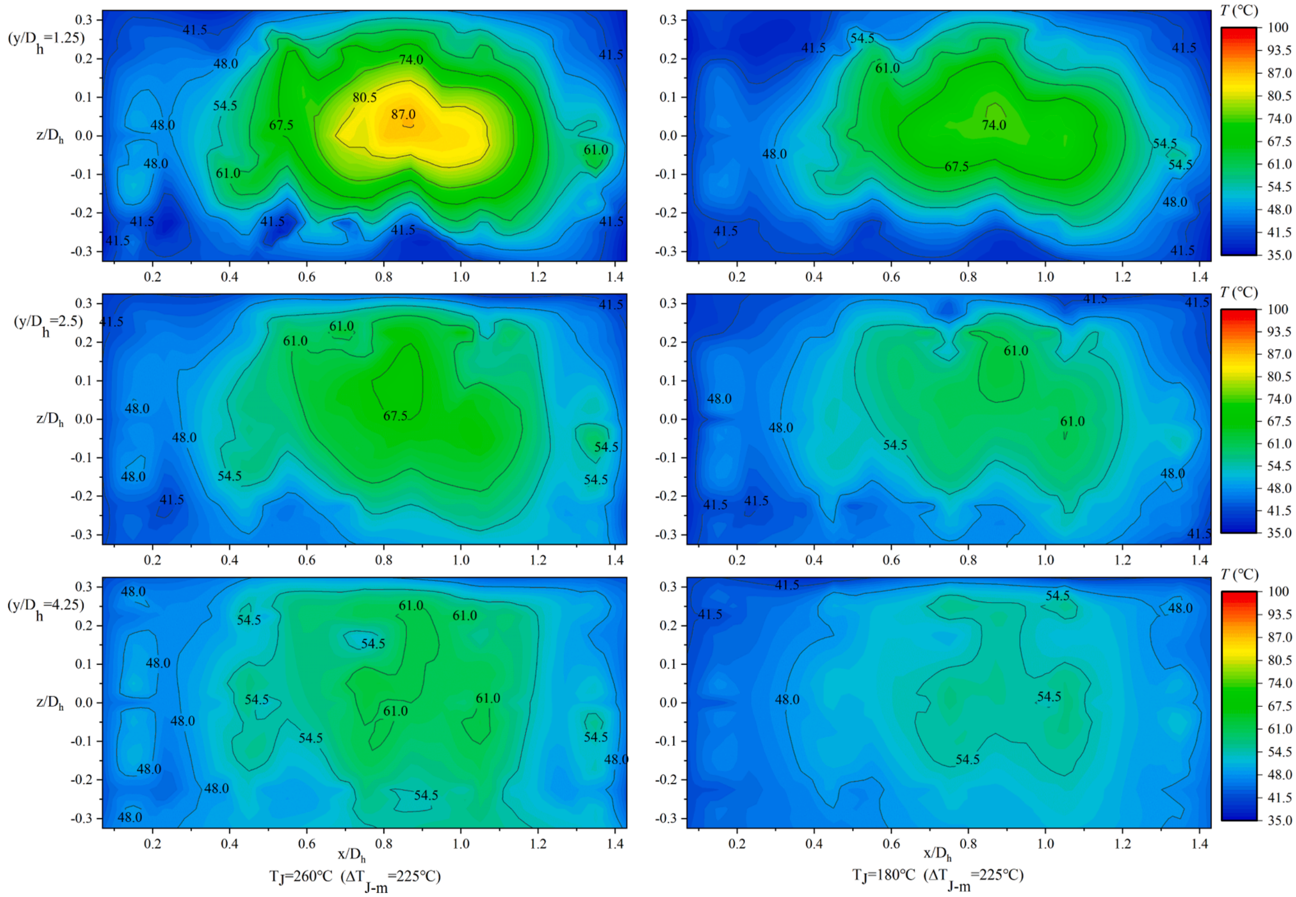

Fig. 16. Temperature distributions for case 4 ($\Delta T_{J\text{-}m}$ = 225℃) and case 5 ($\Delta T_{J\text{-}m}$ = 180℃) at y/D$_h$ = 1.25, y/D$_h$ = 2.5 and y/D$_h$ = 4.25.

results are higher than the values calculated from the experimental results because the number of simulated temperature data points derived within the cross-section is much higher than the number of experimental measurement points. Therefore, the temperature difference in the simulation result statistics is much greater significant than the experimental result, and the calculated ζ_T is inevitably higher than the experimentally calculated result; however, the more the number of data points, the more reliable the calculated results are when used as a reference.

4.3. Effect of flow parameters on thermal mixing features

4.3.1. Effect of the temperature difference between main flow and jet flow on thermal mixing features

Fig. 15 shows the effect of the temperature difference between the mainstream and the jet on the axial temperature after mixing. The

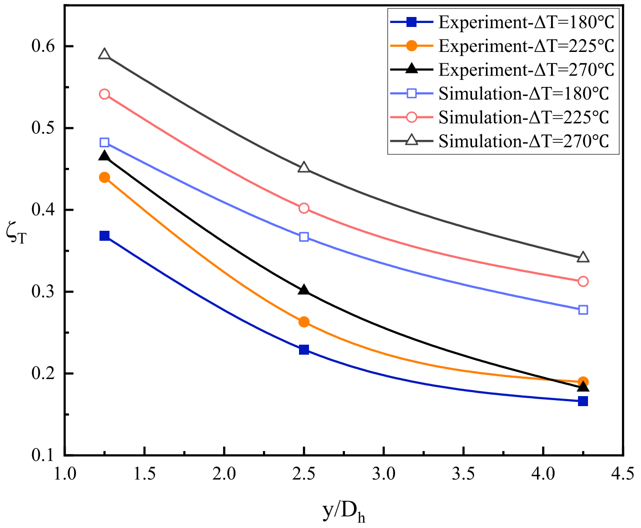

Fig. 17. Effect of jet-to-mainstream temperature difference on temperature mixing non-uniformity.

experimental and simulation results show that the average axial surface temperature after thermal mixing increases with an increase in the jet temperature. When the temperature of the high-temperature jet rises from 215 °C to 305 °C, the warming effect at $y/D_h = 1.25$ increases the surface average temperature from 16.40 °C to 24.98 °C, which is a 52.30 % increase in warming. At $y/D_h = 4.25$, the average surface temperature increases from 14.63 ℃ to 21.68 ℃, which is an increase of 48.15 %.

From Fig. 17, it can be seen that the temperature distribution inhomogeneity coefficient decreases with the temperature difference between the high- and low-temperature flue gases, which means that it decreases with the reduction in the jet temperature for a constant main flow temperature. When the high-temperature jet was reduced from 305 to 215 °C at $y/D_h = 1.25$, ζ_T decreased from 0.4649 to 0.3681, a decrease of 26.29 %. With an increase in the thermal mixing distance, at $y/D_h = 4.25$, ζ_T decreased by only 9.80 %. From Fig. 10 and Fig. 16, it can be observed that as the temperature of the high-temperature jet decreases, the local high-temperature region within the cross-section shrinks and the temperature gradient contour distribution becomes sparser. Therefore, in engineering applications, the location of the bypass flue extraction and the temperature of the extracted gas must be comprehensively considered according to the required warming effect, allowed mixing distance, and temperature deviation range.

4.3.2. *Effect of jet velocity on thermal mixing features*

Fig. 18 shows the effect of different jet velocities on the axial temperature after mixing. The experimental and simulated results showed that the axial average surface temperature after thermal mixing increased with increasing jet velocity. The increase in the jet velocity increases the total enthalpy of the high-temperature gas entering the main flue per unit time, which increases the average surface temperature. Combining Figs. 10 and 19, it can be seen that the areas of the high-temperature and sub-high-temperature regions within the cross-section expand as the jet velocity increases.

The jet trajectory determines the penetration capacity of the jet. Eq. (11) and (12) are typical formulas for describing the trajectory of a jet in a crossflow [40].

$$\frac{y}{R_{eff}\Phi} = A\left(\frac{x}{R_{eff}\Phi}\right)^{B} \rightarrow y = Ax^{B}\left(R_{eff}\Phi\right)^{1-B}\# \tag{11}$$

$$R_{eff} = \sqrt{\frac{\rho_J}{\rho_m}}\left(\frac{U_J}{U_m}\right)\# \tag{12}$$

where U_J and U_m are the jet and main flow speeds separately; ρ_J and ρ_m are the densities of the jet and mainstream gases, respectively, and Φ is the diameter of the jet hole. Parameters A and B are coefficients determined by the experimental conditions, and ρ_J, ρ_m and Φ are kept constant during the experiment. The trajectory of the jet in the main flow was jointly determined by U_J and U_m.

Increasing the jet velocity improves the initial velocity of the jet hole to improve while increasing the initial momentum, which enhances the penetration ability of the jet in the crossflow and reduces the interference of the mainstream with the jet. The most important heat exchange mode in high and low-temperature gas thermal mixing is convection. The mixing of fluids creates a significant disturbance from the vortex generation to their breaking, which results in severe convective heat transfer along with heat conduction and thermal radiation. The penetration ability of the jet improves to avoid being wrapped by the mainstream in the low-speed backflow area formed after the wall. In the low-speed recirculation zone, the generation and breaking of the vortex can be accompanied by forced convective heat transfer, which improves the thermal mixing characteristics of the gas and reduces the temperature distribution non-uniformity coefficient. A jet with a strong penetration ability can retain an intense convection heat exchange effect in the direction of the jet, namely in the axial direction, but does not have a

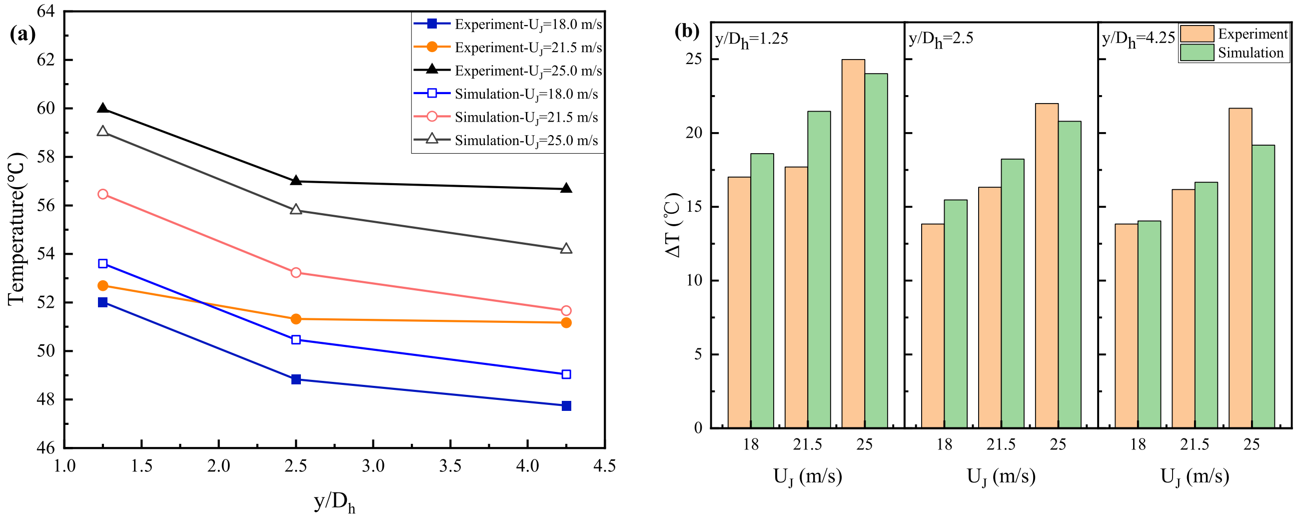

Fig. 18. Effect of jet velocity on the axial temperature after mixing. (a) The average temperature of each section after thermal mixing; (b) the average warming effect of each section after thermal mixing.

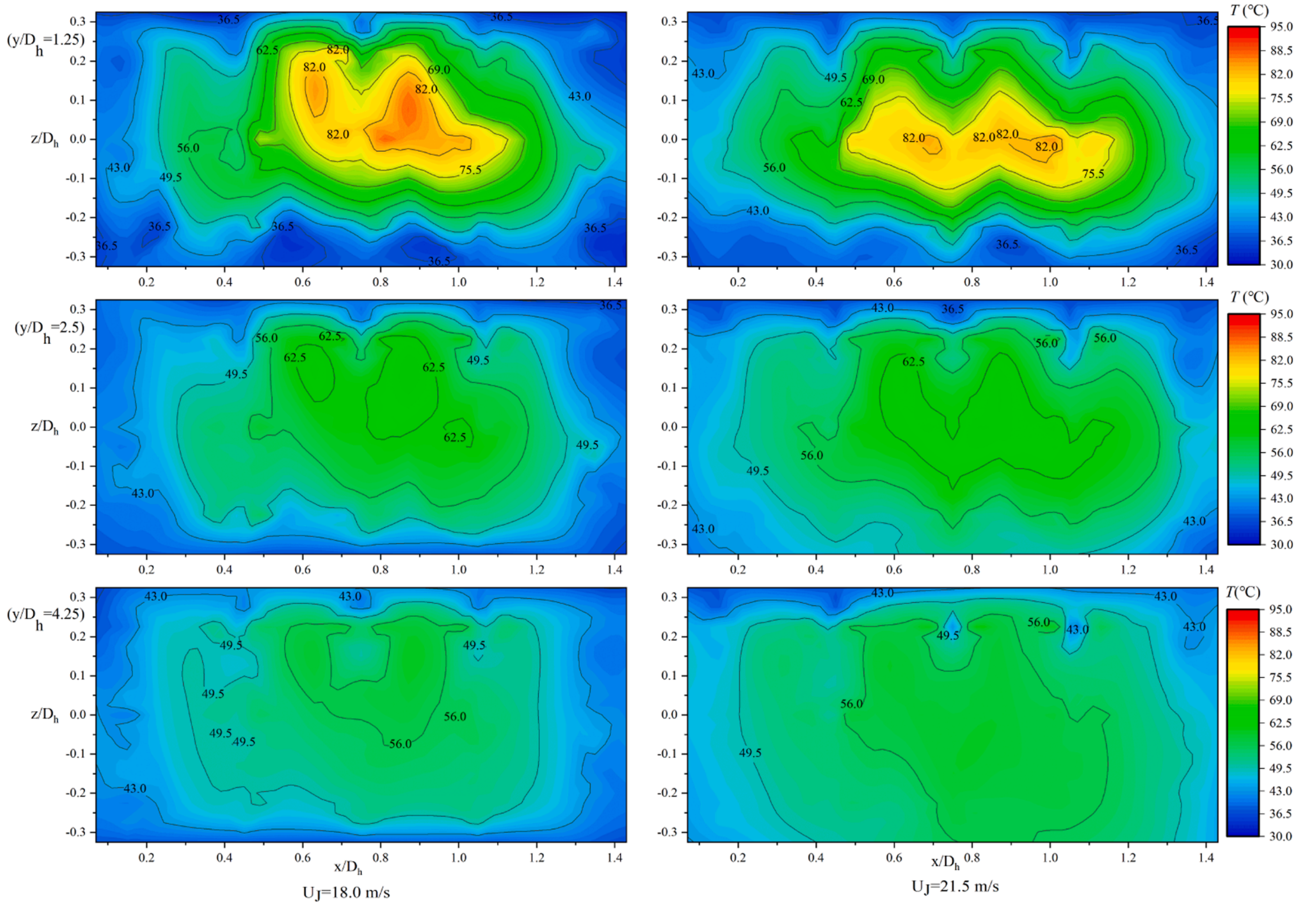

Fig. 19. Temperature distributions for case 6 (U_J = 18.0 m/s) and case 7 (U_J = 21.5 m/s) at y/Dh = 1.25, y/Dh = 2.5 and y/Dh = 4.25.

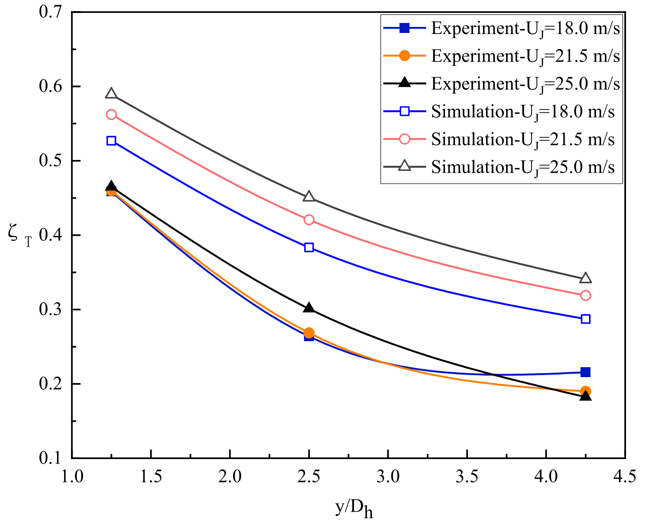

Fig. 20. Effect of jet velocity on temperature mixing non-uniformity.

violent convection effect in the circumferential heat exchange process, and the heat transfer mode is dominated by heat conduction and heat radiation. As a result, the temperature non-uniformity coefficient within the thermal mixing cross-section increases with increasing jet velocity, as shown in Fig. 20.

4.3.3. Effect of main flow velocity on thermal mixing features

Fig. 21 shows the effect of different main flow velocities on the axial temperature after mixing. The experimental and simulation results show that the axial surface temperature decreases after thermal mixing with mainstream velocity improvement. The main flow is low-temperature gas, and the increase in mainstream velocity results in an additional amount of low-temperature gas being thermally mixed with the high-temperature gas per unit time, which reduces the temperature after thermal mixing. However, as shown in Fig. 23, increasing the mainstream velocity can reduce the temperature non-uniformity coefficient after thermal mixing. By combining the temperature distribution contours of case 7 in Fig. 19 and the other cases in Fig. 22, it can be visually observed that as the main flow velocity increases, the local high-temperature zone within $y/D_h = 1.25$ shrinks, the temperature gradient slows down, and the contour distribution becomes sparse.

According to the analysis in Section 4.4, combined with Eqs. (11) and (12), it can be seen that the change in the main flow velocity U_m affects the jet trajectory in the crossflow, resulting in the attenuation of the penetration effect of the jet. Improving the main flow velocity increases the main flow momentum, which enhances the disturbance effect and entrainment ability of the jet and promotes the jet to deflect more quickly into the low-pressure recirculation region behind the tube wall. The high- and low-temperature flue gases produce intense convective heat transfer in the low-pressure recirculation zone, which helps thermal mixing and reduces the temperature inhomogeneity coefficient after mixing.

Combining the results of 4.4 and 4.5 reveals that both the reduction in jet velocity and mainstream speed acceleration can promote the decrease in ζ_T. The velocity ratio, $\frac{U_J}{U_m}$, was changed by the change in the jet and main flow velocities. Therefore, for the process of thermal mixing with a multi-hole jet pipe, the temperature distribution non-uniformity coefficient ζ_T after thermal mixing decreases with a reduction in the

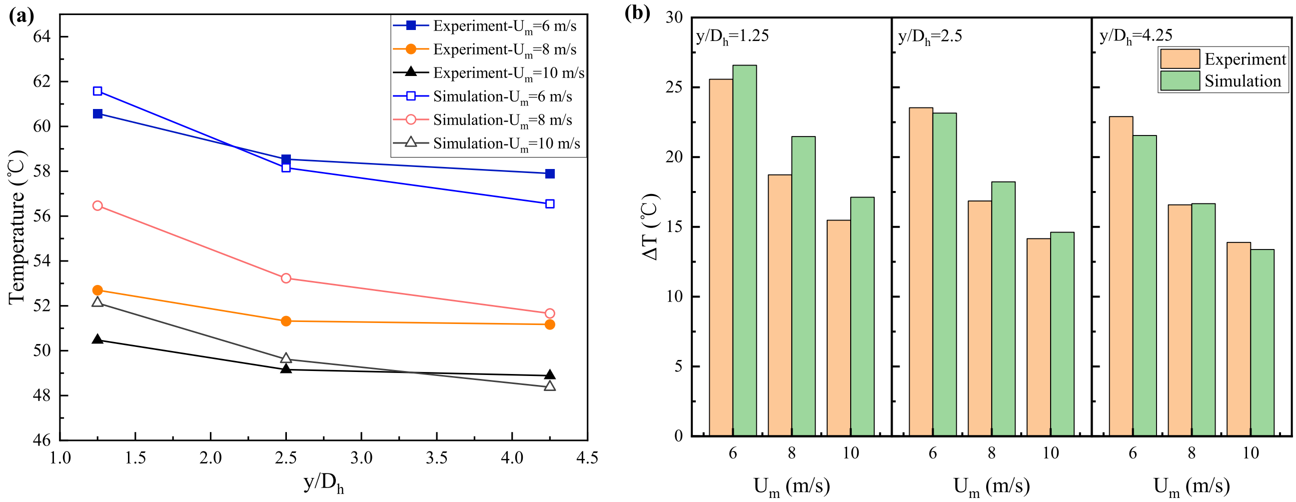

Fig. 21. Effect of main flow velocity on the axial temperature after mixing.

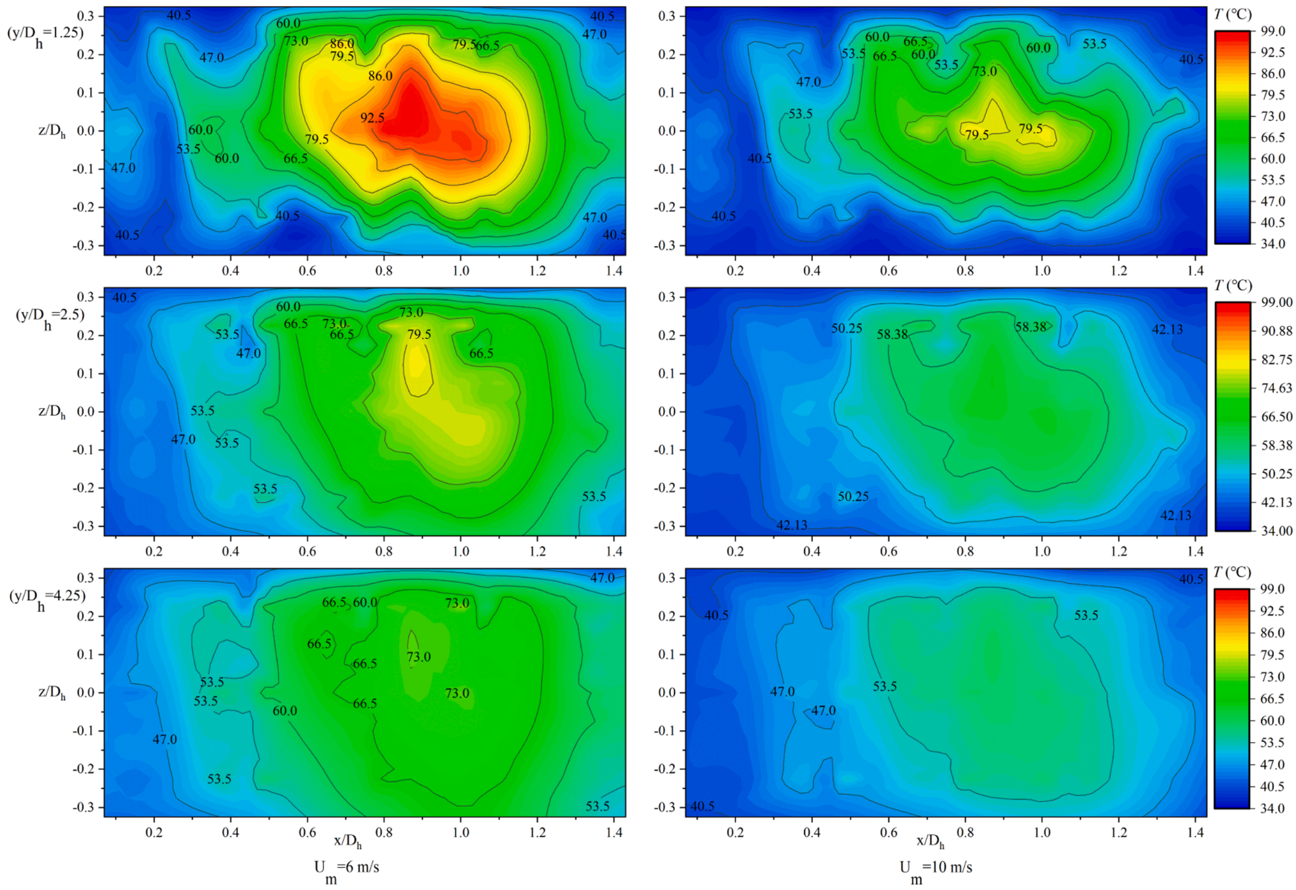

Fig. 22. Temperature distributions for case 8 (U_m = 6 m/s) and case 9 (U_m = 10 m/s) at y/D_h = 1.25, y/D_h = 2.5 and y/D_h = 4.25.

velocity ratio $\frac{U_J}{U_m}$. As shown in Fig. 24, the results of the studies in Sections 4.4 and 4.5 are consistent with this conclusion.

5. Conclusion

In this study, the thermal mixing characteristics of three different high-temperature flue gas injection methods were experimentally investigated using an experimental system that simulated a bypass flue reheat unit at the tail end of a boiler. The flow distribution in the multi-hole jet pipe and the temperature distribution after thermal mixing were measured using a hot-wire anemometer and thermocouples, respectively. By adjusting the temperature difference and flow rate of the main flow and jet, the effect of temperature and flow rate variation on the flue gas thermal mixing characteristics in the main and bypass flues at different low loads were investigated. Numerical simulations of the research work were performed using CFD. The main findings are summarised as follows.

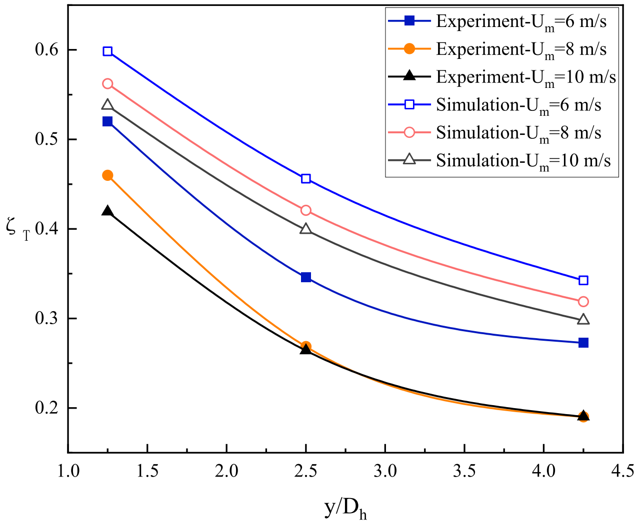

Fig. 23. Effect of main flow velocity on temperature mixing non-uniformity.

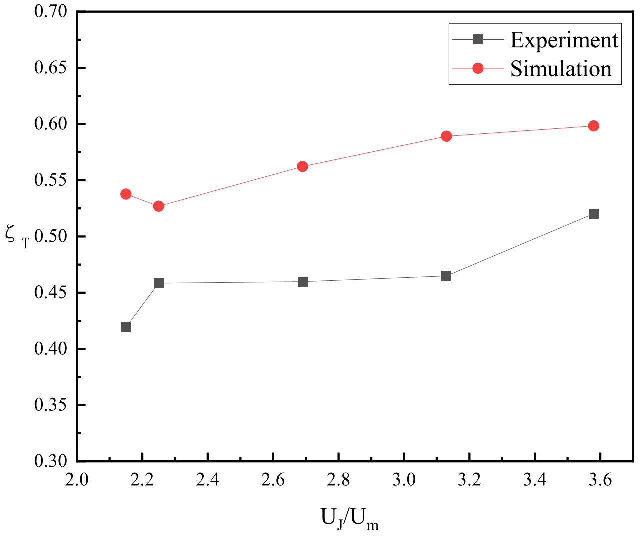

Fig. 24. Effect of velocity ratio $\frac{U_J}{U_m}$ on temperature thermal mixing non-uniformity of $y/D_h = 1.25$ cross-section.

(1) The dimensionless jet velocity of the jet holes of the new multi-hole jet pipe with a hemispherical bottom structure first increases and then decays along the jet direction. The extreme values occur between $x/L = 0.6$ and 0.8 in the middle and rear sections of the jet pipe. The opening of jet holes at the bottom leads to an increase in the deviation of the dimensionless velocity distribution. The main reason for this is that the hemispherical bottom structure creates a large recirculation zone at the back end of the jet pipe, which affects the diversion effect of the jet holes and results in velocity decay.

(2) Among the three different jet mixing methods, type (a) has the highest average surface heating effect and the lowest temperature non-uniformity coefficient of 0.18 after mixing at the $y/D_h = 4.25$ cross-section, indicating the best thermal mixing effect in this method

(3) The inhomogeneity after thermal mixing decreases significantly with a reduction in the temperature difference between the mainstream and the jet. At the $y/D_h = 1.25$ cross-section, when the temperature difference decreases from 270 °C to 180 °C, ζ_T descends from 0.46 to 0.37.

(4) The temperature distribution non-uniformity parameter ζ_T decreases with a reduction in the velocity ratio $\frac{U_J}{U_m}$. For a change in $\frac{U_J}{U_m}$ from 3.58 to 2.15, ζ_T diminishes from 0.52 to 0.42. Adjusting the velocity ratio $\frac{U_J}{U_m}$ improved the non-uniformity of the temperature distribution.

CRediT authorship contribution statement

Yize Zhang: Conceptualization, Methodology, Investigation, Data curation, Writing – original draft, Writing – review & editing. **Mingrui Zhang:** Investigation. **Hao Zhou:** Conceptualization, Methodology, Resources, Supervision, Project administration, Funding acquisition.

Declaration of Competing Interest

The authors declare that they have no known competing financial interests or personal relationships that could have appeared to influence the work reported in this paper.

Data availability

Data will be made available on request.

Acknowledgement

Supported by the Fundamental Research Funds for the Central Universities (2022ZFJH004).

References

[1] Q. Yang, H. Zhou, P. Bartocci, F. Fantozzi, O. Mašek, F.A. Agblevor, Z. Wei, H. Yang, H. Chen, X. Lu, G. Chen, C. Zheng, C.P. Nielsen, M.B. McElroy, Prospective contributions of biomass pyrolysis to China's 2050 carbon reduction and renewable energy goals, Nat. Commun. 12 (2021).

[2] A. Razmjoo, L. Gakenia Kaigutha, M.A. Vaziri Rad, M. Marzband, A. Davarpanah, M. Denai, A Technical analysis investigating energy sustainability utilizing reliable renewable energy sources to reduceCO2 emissions in a high potential area, Renew. Energy, 164(2021) 46-57.

[3] L. Cao, Z. Wang, T. Pan, E. Dong, P. Hu, M. Liu, T. Ma, Analysis on wind power accommodation ability and coal consumption of heat–power decoupling technologies for CHP units, Energy 231 (2021), 120833.

[4] H. Fan, Y. Zhang, Z. Su, B. Wang, A dynamic mathematical model of an ultra-supercritical coal fired once-through boiler-turbine unit, Appl. Energy 189 (2017) 654–666.

[5] M. Zhu, X. Wu, J. Shen, K. Lee, Dynamic modeling, validation and analysis of direct air-cooling condenser with integration to the coal-fired power plant for flexible operation, Energy Convers. Manage. 245 (2021), 114601.

[6] J. Li, J. Wang, Comprehensive utilization and environmental risks of coal gangue: A review, J. Clean. Prod. 239 (2019), 117946.

[7] S. Hu, Y. Ni, Y. Zhang, W. Ma, H. Li, K. Cen, H. Zhou, Visualization research on ash deposition characteristics of Zhundong coal in a vertical liquid slagging cyclone furnace, Fuel Process. Technol. 238 (2022), 107506.

[8] Y. Qiao, S. Li, X. Jing, Z. Chen, S. Fan, Z. Li, Combustion and NO formation characteristics from a 330 MWe retrofitted anthracite-fired utility boiler with swirl burner under deeply-staged-combustion, Energy 258 (2022), 124832.

[9] Z. Zhang, R. Li, M. Wang, Y. Li, Y. Tong, P. Yang, Y. Zhu, Two steps synthesis of CeTiOx oxides nanotube catalyst: Enhanced activity, resistance of SO2 and H2O for low temperature NH3-SCR of NOx, Appl Catal B 282 (2021), 119542.

[10] H. Chen, P. Pan, Y. Wang, Q. Zhao, Field study on the corrosion and ash deposition of low-temperature heating surface in a large-scale coal-fired power plant, Fuel 208 (2017) 149–159.

[11] H. Chen, P. Pan, H. Shao, Y. Wang, Q. Zhao, Corrosion and viscous ash deposition of a rotary air preheater in a coal-fired power plant, Appl. Therm. Eng. 113 (2017) 373–385.

[12] H. Zhou, Y. Ni, Z. Bai, Experimental study on the effects of calcium-based additives to control ammonium bisulfate and ash mixture deposition with an on-line digital image technique, Fuel 286 (2021), 119315.

[13] L. Ma, Q. Fang, P. Tan, C. Zhang, G. Chen, D. Lv, X. Duan, Y. Chen, Effect of the separated overfire air location on the combustion optimization and NO reduction of a 600 MW FW down-fired utility boiler with a novel combustion system, Appl. Energy 180 (2016) 104–115.

[14] X. Zhao, S. Ma, Z. Li, F. Yuan, X. Niu, Y. Zhu, Synthesis of CenTiOx flakes with hierarchical structure and its enhanced activity for selective catalytic reduction of NOx with NH3, Chem. Eng. J. 392 (2020), 123801.

[15] Y. Han, G. Xu, Q. Zheng, C. Xu, Y. Hu, Y. Yang, J. Lei, New heat integration system with bypass flue based on the rational utilization of low-grade extraction steam in a coal-fired power plant, Appl. Therm. Eng. 113 (2017) 460–471.
[16] X. Zhang, Z. Chen, M. Zhang, L. Zeng, Z. Li, Combustion stability, burnout and NO emissions of the 300-MW down-fired boiler with bituminous coal: Load variation and low-load comparison with anthracite, Fuel 295 (2021), 120641.
[17] H. Du, Z. Li, Z. Liu, M. Zhang, C. Huang, G. Jiang, Z. Chen, J. Song, F. Fang, J. Su, H. Liu, Industrial measurement of combustion and NOx formation characteristics on a low-grade coal-fired 600MWe FW down-fired boiler retrofitted with novel low-load stable combustion technology, Fuel 321 (2022), 123926.
[18] R.M. Kelso, T.T. Lim, A.E. Perry, An experimental study of round jets in cross-flow, J. Fluid Mech. 306 (1996) 111–144.
[19] L.K. Su, M.G. Mungal, Simultaneous measurements of scalar and velocity field evolution in turbulent crossflowing jets, J. Fluid Mech. 513 (1999) 1–45.
[20] V.S. Naik-Nimbalkar, A.D. Suryawanshi, A.W. Patwardhan, I. Banerjee, G. Padmakumar, G. Vaidyanathan, Twin jets in cross-flow, Chem. Eng. Sci. 66 (2011) 2616–2626.
[21] S. Ghahremanian, K. Svensson, M.J. Tummers, B. Moshfegh, Near-field mixing of jets issuing from an array of round nozzles, Int. J. Heat Fluid Flow 47 (2014) 84–100.
[22] C. Choi, W. Choi, J.H. Choi, D. Shin, Penetration behavior of opposed rows of staggered secondary air jets depending on jet penetration coefficient and momentum flux ratio, Int. J. Heat Mass Transf. 101 (2016) 274–279.
[23] W. Zhou, K. Xing, S. Dou, Q. Yang, X. Xu, Experimental and numerical investigations on the mixing process of supercritical jet injected into a supersonic crossflow, Aerospace 9 (2022) 631.
[24] L. Wang, L. Zhang, W. Lin, Y. Wu, X. Wu, Spray trajectory and 3D droplets distribution of liquid jet in crossflow with digital inline holography, Exp. Therm. Fluid Sci. 139 (2022), 110725.
[25] Y. Lv, H. Wei, T. Liu, X. Zhao, Y. Liu, B. Huang, G. Wang, Numerical investigation of the round jet in crossflow at high velocity ratios with special emphasis on the evolution of vortex structures, Phys. Fluids 34 (2022) 34116.
[26] A.M. Steinberg, R. Sadanandan, C. Dem, P. Kutne, W. Meier, Structure and stabilization of hydrogen jet flames in cross-flows, Proc. Combust. Inst. 34 (2013) 1499–1507.
[27] J. O'Connor, V. Acharya, T. Lieuwen, Transverse combustion instabilities: Acoustic, fluid mechanic, and flame processes, Prog. Energy Combust. Sci. 49 (2015) 1–39.
[28] H. Zhou, C. Tao, Effects of annular N2/O2 and CO2/O2 jets on combustion instabilities and NOx emissions in lean-premixed methane flames, Fuel 263 (2020), 116709.
[29] B. Stiehl, A. Morales, T. Genova, M. Otero, S. Martin, C. Yoon, K. Ahmed, Controlling pollutant emissions in a high-pressure combustor with fuel-diluent blending, Fuel 317 (2022), 123481.
[30] M.D. Sirignano, V. Nair, B. Emerson, J. Seitzman, T.C. Lieuwen, Nitrogen oxide emissions from rich premixed reacting jets in a vitiated crossflow, Proc. Combust. Inst. 37 (2019) 5393–5400.
[31] C. Tao, H. Zhou, Effects of superheated steam on combustion instability and NOx emissions in a model lean premixed gas turbine combustor, Fuel 288 (2021), 119646.
[32] M. Fraas, T. Glasenapp, A. Schulz, H. Bauer, Optimized inlet geometry of a laidback fan-shaped film cooling hole – Experimental study of film cooling performance, Int. J. Heat Mass Transf. 128 (2019) 980–990.
[33] H. Zhu, G. Xie, R. Zhu, B. Sunden, Comparisons on flow characteristics and film cooling performance of cylindrical and sister holes with/without internal coolant crossflow, Int. J. Therm. Sci. 182 (2022), 107791.
[34] H. Ding, C. Zhuo, X. Chen, H. Deng, M. Li, B. Sun, C. Li, Numerical study on the transverse jet flow and mixing characteristics of hydrogen/metal powder fuel in powder fuel scramjet, Fuel 326 (2022), 125088.
[35] H. Zhou, J. Chen, M. Zhou, K. Cen, Experimental investigation on the mixing performance of heating gas into the low temperature sintering flue gas selective catalyst reaction facilities, Appl. Therm. Eng. 115 (2017) 378–392.
[36] X. Guo, H. Zhou, H. Shi, Y. Li, K. Zhang, M. Zhou, Promotion of the mixing performance of heated gas and low-temperature sintering gas in selective catalytic reaction facilities, Exp. Therm. Fluid Sci. 94 (2018) 258–280.
[37] S. Hu, Y. Ni, Q. Yin, J. Wang, L. Lv, K. Cen, H. Zhou, Research on element migration and ash deposition characteristics of high-alkali coal in horizontal liquid slagging cyclone furnace, Fuel 308 (2022), 121962.
[38] F. Lu, Y. Luo, S. Yang, Analytical and experimental investigation of flow distribution in manifolds for heat exchangers, J. Hydrodynam. Ser. B 20 (2008) 179–185.
[39] P. Luo, H. Jia, C. Xin, G. Xiang, Z. Jiao, H. Wu, An experimental study of liquid mixing in a multi-orifice-impinging transverse jet mixer using PLIF, Chem. Eng. J. 228 (2013) 554–564.
[40] M.T. Kandakure, V.C. Patkar, A.W. Patwardhan, J.A. Patwardhan, Mixing with jets in cross-flow, Industr. Eng. Chem. Res. 48 (2009) 6820–6829.